Materials Science and Engineering B 322 (2025) 118673

Contents lists available at ScienceDirect

Materials Science & Engineering B

journal homepage: www.elsevier.com/locate/mseb

Growth and characterization of orthorhombic cesium lead tri-iodide perovskite thin-films by sequential physical vapor deposition for solar cells

Sizwe Sibiya , Mmantsae Diale *

Department of Physics, University of Pretoria, Private Bag X20, Pretoria 0028, South Africa

ARTICLE INFO

Keywords:
Cesium lead triiodide
Inorganic solar cell
Perovskite
Trap states
Sequential physical vapour deposition

ABSTRACT

This study used the sequential physical vapor deposition (SPVD) technique to grow poly-crystalline yellow phase cesium lead triiodide (γ-$CsPbI_3$). The effect of CsI thickness on structural, optical, morphological, and electrical properties of γ-$CsPbI_3$ was investigated. Crystallographic parameters of γ-$CsPbI_3$ as-deposited and 100 °C annealed pure-phase were determined using X-ray diffraction (XRD). Computed lattice constants were a = 4.88, b = 9.96, and c = 16.5 Å, with an average crystallite size increasing from 170 − 243 nm, and micro-strain decreasing with an increase of cesium iodide (CsI) thickness from 200 to 500 nm. Field-emission scanning electron microscopy (FE-SEM) images showed uniform surface coverage with polycrystalline grains. Average grain size increased from 168 to 235 nm with increasing CsI thickness, resulting in large, pinhole-free, and tightly packed grains. Furthermore, atomic force microscopy (AFM) surface analysis demonstrated a reduction in surface roughness from 44.0 to 38.3 nm as CsI thickness increased from 200 to 500 nm. The ultraviolet–visible (UV–Vis) spectra showed an increase in bandgap from 2.24 to 2.38 eV for as-deposited and a decrease from 2.37 to 2.05 eV for annealed films as the thickness of CsI increased. Current–voltage (J-V) measurements revealed a correlation between the trap-filled limit voltage (V_{TFL}) and defect density. For electron-only devices with film thicknesses of 300, 400, 500, and 600 nm, the trap state densities were found to be 1.40×10^{15}, 1.95×10^{15}, 2.12×10^{15}, and 2.39×10^{15} cm^{-3}, respectively. The corresponding electron mobilities were 2.34×10^{1}, 6.30×10^{1}, 4.72×10^{2}, and 1.07×10^{2} $cm^2/V{\cdot}s$. Additionally, perovskite solar cells (PSCs) fabricated under ambient air conditions revealed an improvement in power conversion efficiency (PCE) from 2.0 to 4.93 % for the FTO/c-TiO_2/$CsPbI_3$/Au architecture. This work suggests a way of improving precursor's reaction using SPVD by controlling the film thickness, reducing defect density through SPVD, and therefore highlighting film thickness optimization in perovskites.

1. Introduction

Organic-inorganic perovskite (OIP) semiconductors have drawn significant attention since their emergence due to excellent optoelectronic properties, which include a large optical absorption range [1], low phonon energy [2], low exciton binding energy [3], tunable bandgap [4], long carrier diffusion length [5]. These materials have found applications in batteries [6], high-energy radiation detectors [7], gas sensors [8], and particularly in solar cells [9]. Over the past decade or so, the PCE of traditional OIP-based solar cells improved significantly from 3.80 to over 25 % [10] approaching the performance of commercial monocrystalline silicon (26.7 % PCE) and outperforming copper indium gallium selenide (Cu(In, Ga)Se2) based solar cells (22.9 % PCE).

Despite these advancements, instability remains a major barrier to the commercialization of PSCs, which typically have a lifetime of about 3000 h [11], far less than the 25-year lifespan of commercially available silicon solar cells. Instability arises from various factors, including exposure to ultraviolet radiation [12], humidity [13], film quality [14], stoichiometry [15], and structure [16].

To address these challenges, researchers have explored strategies such as compositional engineering and architectural modifications [17,18]. Replacing the volatile organic A-site cation (e.g., methylammonium, MA^+) with inorganic cesium (Cs^+) has proven effective in enhancing thermal and structural stability [19,20]. Jiang et al. [21] investigated the degradation of methylammonium lead tri-iodide ($MAPbI_3$), formamidinium lead tri-iodide ($FAPbI_3$), formamidinium methylammonium lead tri-iodide ($FA_{0.6}MA_{0.4}PbI_3$), and formamidinium cesium lead tri-iodide ($FA_{0.9}Cs_{0.1}PbI_3$) labelled as MA, FA, FM, and FC,

* Corresponding author.
E-mail address: mmantsae.diale@up.ac.za (M. Diale).

https://doi.org/10.1016/j.mseb.2025.118673
Received 29 January 2025; Received in revised form 29 July 2025; Accepted 3 August 2025
Available online 7 August 2025
0921-5107/© 2025 The Author(s). Published by Elsevier B.V. This is an open access article under the CC BY-NC license (http://creativecommons.org/licenses/by-nc/4.0/).

respectively, under thermal cycles between 30 and 85 °C. Notable degradation of open-circuit voltage (Voc), short-circuit current (Jsc), fill factor (FF), and PCE was observed in MA, FA, and FM devices due to phase transitions. In contrast, the FC device showed successful suppression of defects, resulting in improved stability. Grain boundaries (GBs) also reduce performance and cause degradation due to defects such as pinholes that facilitate degradation, which begins at the surface and penetrates the film [22,23]. Castro-Mendez et al. [24] showed that degradation begins at grain boundaries due to lattice mismatch and defects, highlighting the need for large, compact grains to ensure stability. Although traditional organic A-site perovskites exhibit strong visible absorption [25] and high efficiencies [26], inorganic Cs-based perovskites offer superior environmental robustness and are particularly promising for tandem cell applications due to their compatibility with silicon and high external quantum efficiency [27,28].

$CsPbI_3$, one of the most studied all-inorganic perovskites, exhibits a suitable small bandgap (~1.6–1.72 eV), owing to its high PCEs above 20 % [29], while the mixed halide has ~1.82 – 2.5 eV with low PCEs below 13 % [30]. Most studies reporting on high PCEs based on Cs A-site cation perovskite devices use solution-based synthetic techniques [31]. However, the resulting thin film's morphology is often non-uniform with inconsistent phase purity and irreproducible. Vapor-phase techniques, particularly co-evaporation, allow better control over film stoichiometry and purity, but are limited by complexity in managing precursor evaporation rates [32] and deposition conditions [33]. For instance, fluctuations in the evaporation rates can lead to off-stoichiometric films, resulting in the formation of unwanted secondary phases and defects that degrade device performance. Moreover, co-evaporation requires complex equipment setups with multiple sources and real-time monitoring systems to adjust the deposition rates, increasing the complexity and cost of the fabrication process. In contrast, the SPVD method involves the sequential deposition of PbI_2 followed by CsI, allowing for independent control over the thickness and deposition rate of each layer. This sequential approach simplifies the deposition process, reduces equipment complexity, and enhances reproducibility. By carefully controlling the deposition parameters and annealing conditions, we achieved phase-pure γ-$CsPbI_3$ films with improved crystallinity and uniformity.

In this study, SPVD-fabricated films exhibited superior optoelectronic properties, including reduced trap-state densities and enhanced charge transport characteristics, compared to films produced by traditional co-evaporation methods [34]. These improvements underscore the potential of SPVD as a scalable and reproducible technique to fabricate high-performance, stable perovskite solar cells.

2. Experimental

2.1. Materials

Ethanol (99.5 %), Isopropanol (99.5 %), acetone (99.5 %), TTIP (99,999 %), PbI_2 (99.9 %), CsI (99.9 %), lithium fluoride LiF (95.6 %), and Au (99 %) from Sigma Aldrich were used as received.

2.2. Substrate cleaning

Fluorine-doped Tin Oxide (FTO) glass substrates were cleaned by ultrasonication in acetone (15 mL), isopropanol (15 mL), and deionized H_2O (15 mL) for 10 min at 30 °C each to remove surface contamination, then dried under nitrogen gas.

2.3. c-TiO_2 electron transport deposition

Compact titanium dioxide (c-TiO_2) thin films were grown via spray pyrolysis as shown in Fig. 1(a). The precursor solution was prepared by mixing 7.4 mL of TTIP with 50 mL of ethanol and stirring for 10 min. Before deposition, FTO substrates were pre-heated to 300 °C. The solution was sprayed using a vertical spray gun positioned 30 cm above for 5 s (for 20 nm thickness), maintaining substrate temperature. After coating, the films were cooled to room temperature, transferred to a tube furnace, annealed at 450 °C for an hour, and left to cool overnight.

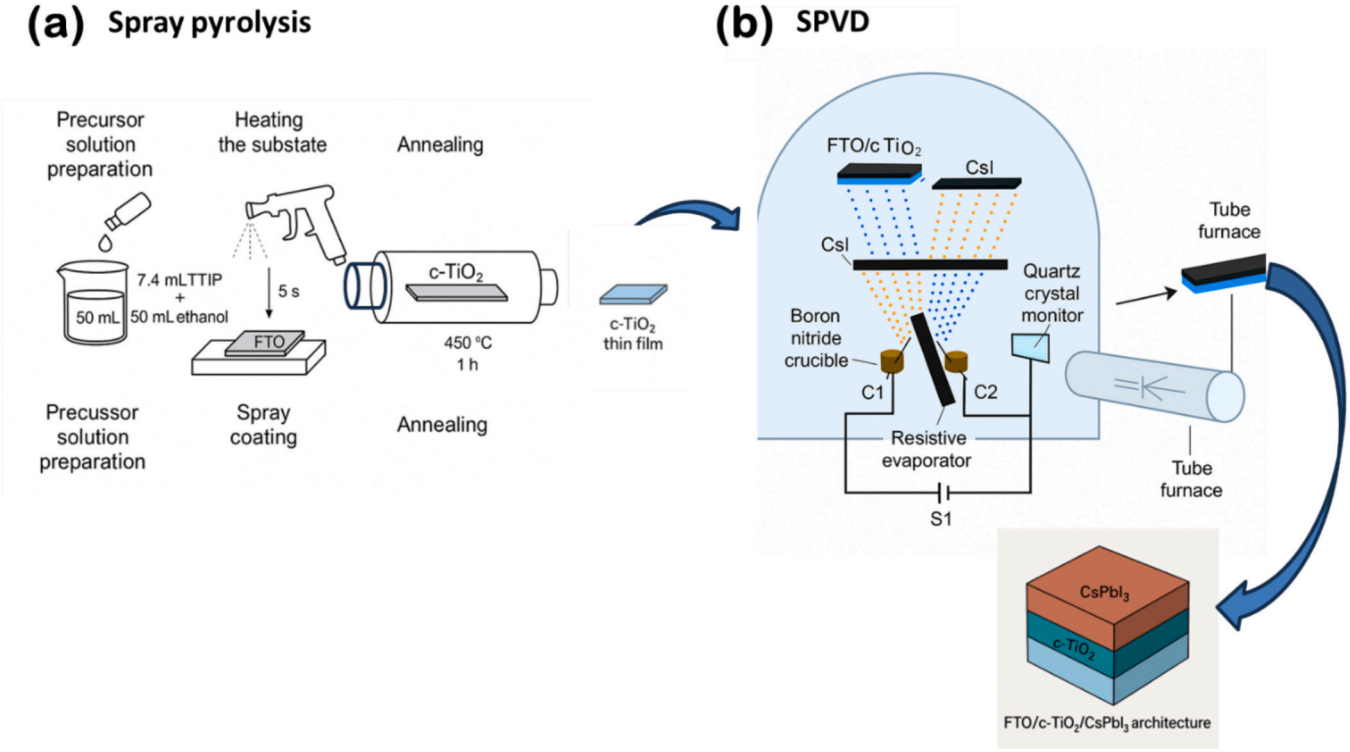

Fig. 1. (a) Schematic of spray pyrolysis deposition of c-TiO_2 thin films on heated FTO substrates, followed by annealing at 450 °C. (b) Illustration of the resistive evaporator demonstrating sequential deposition of PbI_2 and CsI precursors.

2.4. $CsPbI_3$ perovskite film deposition

The preparation of $CsPbI_3$ was achieved using SPVD as depicted in Fig. 1(b). Cleaned FTO substrates were loaded into the resistive evaporator to ensure a controlled deposition environment. PbI_2 and CsI powders were placed in separate boron nitride crucibles (C1 and C2) in the vacuum chamber. The PbI_2 thickness was fixed at 100 nm, while CsI varied from 200 – 500 nm in 100 nm steps. The thickness was monitored using a quartz crystal monitor positioned at the same level as the mounted glass/FTO substrates. Samples were then transferred into a tube furnace and annealed for 10 min in open air.

2.5. FTO/c-TiO_2/$CsPbI_3$/LiF/Au fabrication

As discussed above, electron-only devices were fabricated with c-TiO_2 (20 nm) and varying $CsPbI_3$ thicknesses (300, 00, 500, and 600 nm). Subsequently, a 20 nm layer of lithium fluoride (LiF) was thermally evaporated onto the perovskite, and the device was completed with an 80 nm gold (Au) electrode.

2.6. FTO/c-TiO_2/$CsPbI_3$/Au fabrication

The above device fabrication process was repeated with 20 nm molybdenum Oxide (MoO_3) replacing LiF, followed by an 80 nm layer of Au. The electrical performance of both device types was evaluated using I-V measurements with an Agilent B2912A Source Measure Unit, under illumination from an ORIEL LCS-100 solar simulator equipped with an AM 1.5 G filter and calibrated with a Newport 91150 V silicon reference cell.

2.7. Characterization

The Bruker D2-Phaser XRD was used to evaluate the thin films' structural properties using Cu Kα radiation with a wavelength of 1.5405 Å. The angle 2θ between the incident and diffracted rays was varied in steps of 0.05° from 10° to 50°. The film's structure, crystal size, crystallinity, dislocation density, and residual strain of the films were analysed using diffractogram data. FE-SEM was used to examine the film's morphology (FE-SEM, Zeiss Crossbeam 540). ImageJ software was used to analyse the grain size on the FE-SEM micrographs using the American Standard for Testing and Materials (ASTM). AFM surface roughness analysis was conducted using a Park Scientific Autoprobe CP (Park Scientific Instruments, Sunnyvale, CA) with an AFM/LFM head. Topography images were captured in constant force mode, using minimal force to maintain contact between the tip and the sample. A rectangular 'Microlever' cantilever with a nominal force constant was employed for the measurements. The films' optical absorption spectra were assessed using a CARY-60 BIO UV–vis spectrometer with incident light wavelengths ranging from 400 to 800 nm.

3 Results

3.1 Structural properties

The XRD diffractograms of $CsPbI_3$ thin films grown on glass/FTO as-deposited and annealed at 100 °C are shown in Fig. 2(a) and (b). Crystallinity of the films was studied from the sharply varying peak intensities for the deposited 100 nm PbI_2 with varying thickness of CsI from 200 – 500 nm. Orthorhombic-phase crystal structure was confirmed with 2θ peaks at 21.04°, 26.69°, 27.84°, 33.67°, 37.91°, 41.66°, 46.01°, 48.74° and 51.69° corresponding to the crystallographic planes (111), (121), (122), (101), (132), (200), (117), (114), (201), and (211), respectively. Calculated lattice constants of the structure were a = 4.88 Å, b = 9.96 Å, and c = 16.5 Å, confirmed by the JCPDS – card no 74–970, and in good agreement with the yellow optically active γ-$CsPbI_3$. Furthermore, the peak displayed at 2θ = 12.92° with (0 0 1) crystallographic plane was confirmed to be unreacted PbI_2-residue according to the JCPDS card no 07-0235. This peak reduced with an increase in CsI thickness, showing the phase-purity of $CsPbI_3$ to increase with an increase in CsI. The intensities of (1 2 2) and (1 3 2) diffraction planes increase with CsI thickness as shown in Fig. 2(a) and (b), indicating an increase in crystallinity of γ-$CsPbI_3$. This phenomenon may be due to the increment of iodide and cesium required at Wycoff positions in the crystal lattice, thereby improving the structure factor. Additionally, the rise in peak intensity can be attributed to the increased number of reflection planes, which raises the multiplicity factor and, as a result, the intensity. This may also be due to coherent scattering caused by an additional layer of atoms, leading to the upsurge of the diffraction peak intensities.

Researchers are not in agreement on whether the excess of PbI_2 could

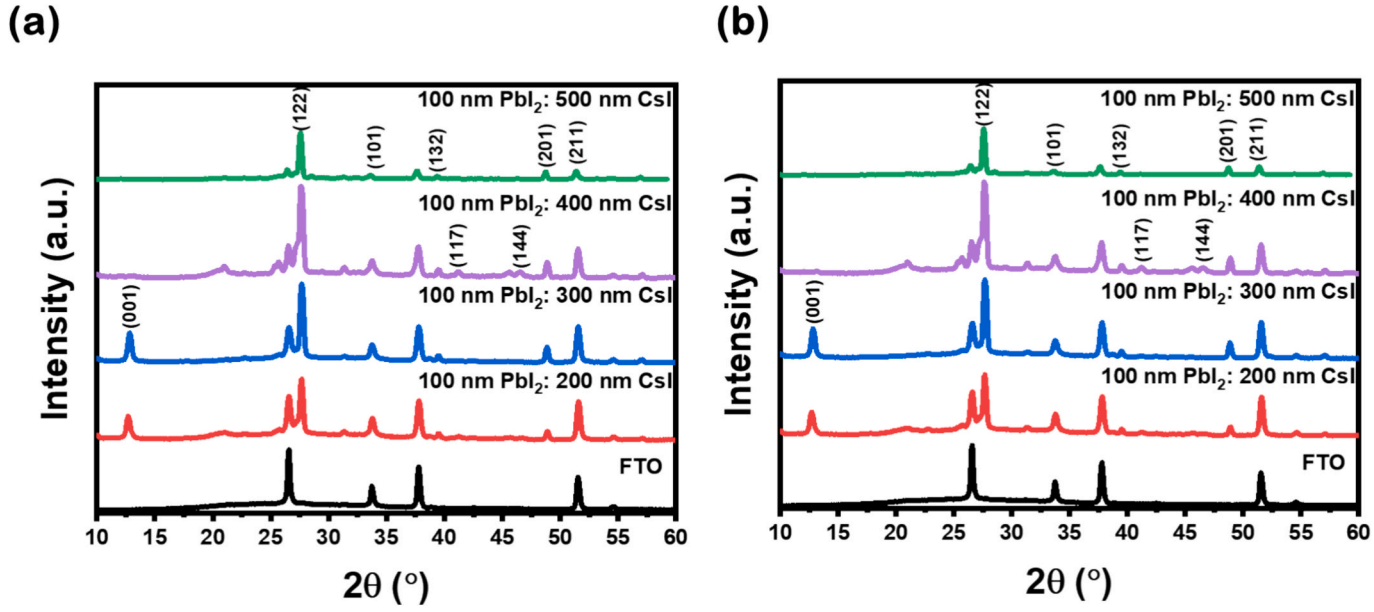

Fig. 2. XRD patterns of γ-$CsPbI_3$ thin films with varying CsI thicknesses (200 – 500 nm): (a) as-deposited films and (b) annealed at 100 °C. Reflection patterns demonstrated an orthorhombic-phase crystallinity.

have a positive or negative impact on PSCs. Yang et al. discovered that residual PbI_2 located at the grain boundaries, near the surface of the perovskite, between the charge transport layers, and the perovskite, facilitates passivation of defects while improving optoelectronic properties of the perovskites [35]. On the contrary, Alberti et al. showed that excess PbI_2 under illumination decomposes to Pb^0 and I_2 crystals, allowing Pb^0 to slow down crystallization while increasing non-radiative recombination, consequently compromising the overall stability and durability of the solar cell [36]. In this study, we observe excess PbI_2 suppression precisely from 300 – 500 nm CsI thicknesses by the gradual decrease of the peak depicted in Fig. 2(a) and (b), defined as $2\theta = 12.92^{\circ}$.

Furthermore, the XRD diffractograms in Fig. 2(a) for as-deposited 200 – 300 nm CsI suggest incomplete growth of as-deposited γ-$CsPbI_3$, likely due to high traces of PbI_2. However, a 400 nm CsI thickness thin film suggests complete conversion to $CsPbI_3$ with reduced traces of PbI_2 peak, thus confirming that a 1:4 stoichiometric ratio of PbI_2:CsI thicknesses is optimal for producing a pure phase 500 nm γ-$CsPbI_3$ thin film. Crystallite size and the micro-strains resulting from crystal defects were studied using Debye-Scherrer and modified Williamson-Hall methods, respectively. Equation (1) shows the Williamson-Hall formula:

$$\beta cos\theta = \frac{K\lambda}{D} + 4\varepsilon sin\theta \tag{1}$$

where λ is the wavelength, ε is the micro-strain, θ is the Bragg's diffraction angle, D is the average crystallite size, and $K = 2\sqrt{(ln2)/\pi}$ is the Scherer constant is determined by using the crystallite shape, and is considered as 0.94 for spherical crystallites with cubic symmetry. The micro-strain and crystallite size were determined by a constant multiplied by the reciprocal of the intercept, which correlates with the W-H plot (*FWHM*cos (θ) vs. 4sin (θ)) of the $CsPbI_3$ diffractograms, as depicted in Fig. 4(a) and (b). It is observed that micro-strain decreases with increasing CsI thickness. Zhao et al. [45] demonstrated that a reduction in micro-strain flattens the valence band and, as a result, enhances hole extraction at the perovskite/hole interface layer. Additionally, they observed that the removal of micro-strains results in enhanced carrier mobility. However, Jones et al. [46] pointed out that micro-strain enhances non-radiative recombination by promoting defect concentration. Therefore, it is expected that the reduction in micro-strain will decrease non-radiative recombination because of low defect density. The calculated average crystallite size increased from 127 to 243 nm with increasing CsI thickness as shown in Fig. 4(b), and the increase may be due to a decrease in micro-strain, which is expected to cause a decrease in bandgap.

Compressive stress observed in Fig. 4(a) correlates with the least dislocation density shown in Fig. 5(b), for 400 nm CsI thin film, as-deposited. The positive slope indicates compressive strain. This could be due to mechanical and thermal treatment (in the bell jar) facilitating large crystallites during $CsPbI_3$ growth [47]. However, in annealed thin films, both mechanical and thermal stress impose tensile strain. This is because mechanical fabrication and thermal annealing aim to minimize interface, surface, and grain boundary (GB) energies during grain growth [48]. Additionally, crystals grown by the SPVD technique are expected to improve compressive stress attributed to the film quality, surface coverage [49], and complete interdiffusion of the precursors.

Lattice constants of the orthorhombic crystal structure were determined using Bragg's law, Equation (2), and Miller indices of an orthorhombic crystal structure given by Equation (3),

$$n\lambda = 2dsin\theta \tag{2}$$

where $n = 1$ and spacing d is the distance between the planes of atoms.

$$\frac{1}{d_{hkl}^2} = \frac{h^2}{a^2} + \frac{k^2}{b^2} + \frac{l^2}{c^2} \tag{3}$$

where a, b, and c represent the lattice constants, and (hkl) denotes the Miller indices. These lattice constants were derived from experimental data for the all-inorganic crystals for varied CsI thicknesses, as shown in Table 1. Wang and co-workers [37], showed that the room-temperature yellow-phase γ-$CsPbI_3$ suffers from lattice distortion and structural degradation. In addition, they demonstrated that the degree of lattice distortion from α-$CsPbI_3$, β-$CsPbI_3$, to γ-$CsPbI_3$ relates to dislocation density. Fig. 4(b) shows films with low CsI thicknesses (200——300 nm) exhibiting higher dislocation density, thus distorted lattice constants. Furthermore, a 400 nm CsI thickness film, which displayed better crystallinity in Fig. 3(a) and (b), demonstrates low dislocation density. This suggests a reduction in non-radiative recombination because of low defect densities. Liu et al. [38], showed that γ-$CsPbI_3$ (yellow phase, Eg ~ 2.8 eV) inorganic isomer of the cubic α-$CsPbI_3$ (black phase, Eg ~ 1.7 eV), exhibits a poor response to the solar spectrum due to structural dislocation.

The dislocation density, denoted as ρ, is related to the crystallite size by Williamson-Smallman formula [39] given in Equation (4),

$$\rho = \frac{n}{D^2} \tag{4}$$

where n equals unity for minimum dislocation density. The calculated dislocation density is illustrated in Fig. 4(b), and the results indicate a

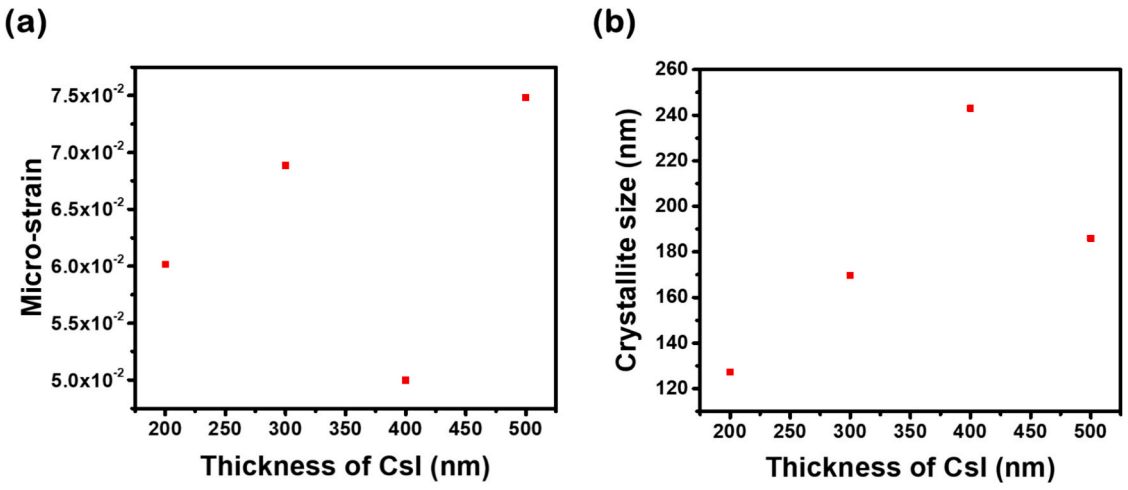

Fig. 3. (a) Variation of micro-stain as a function of CsI thickness, demonstrating consistent reduction with increasing CsI thicknesses. (b) Average crystallite size determined using the William-Hall method, showing grain growth as CsI thickness increases.

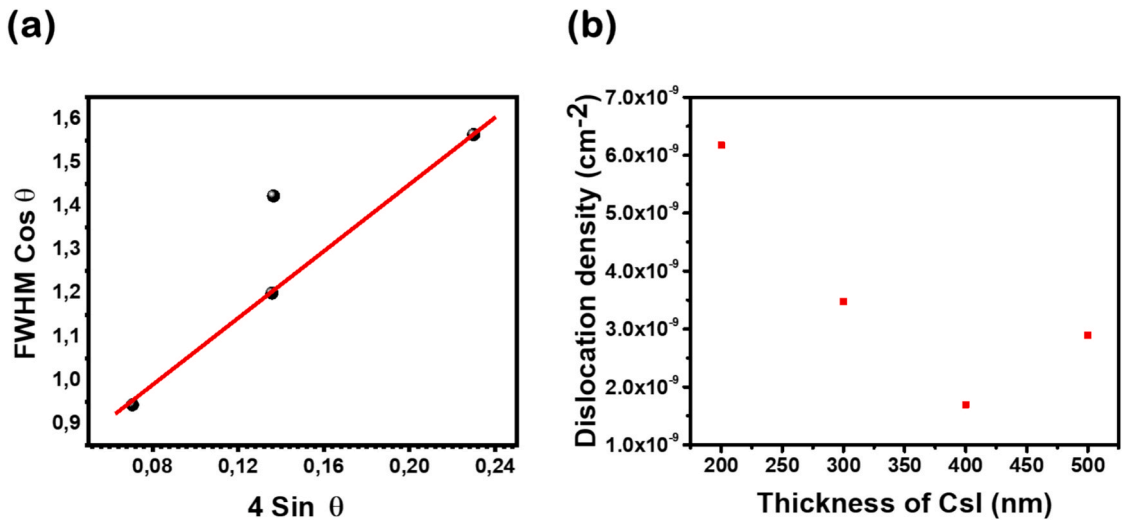

Fig. 4. (a) Linear trend demonstrating increasing internal stress with thicker CsI films calculated from the shift in XRD peak positions relative to strain-free references. (b) Dislocation density of γ-$CsPbI_3$ thin films grown with varying CsI thickness.

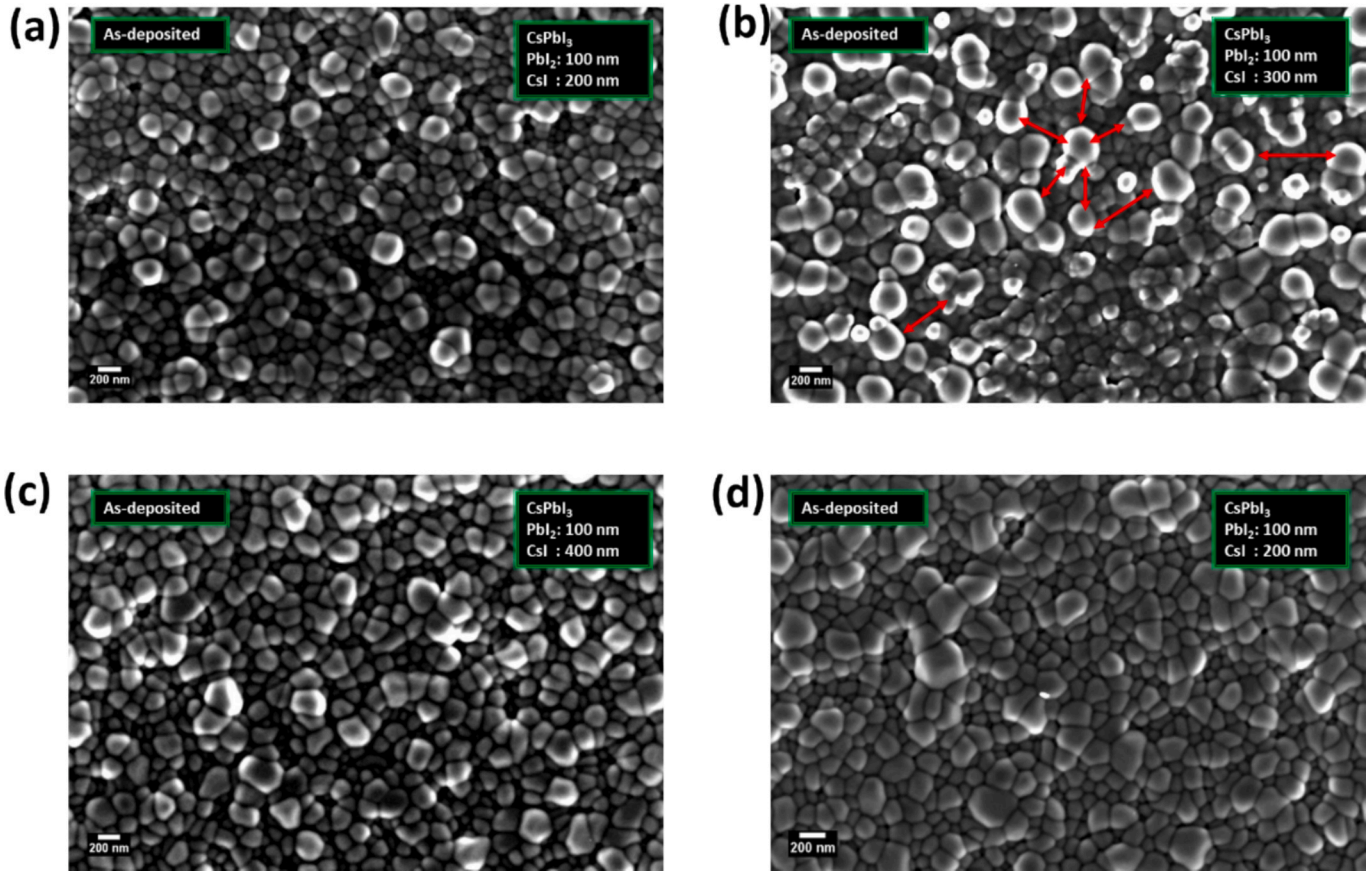

Fig. 5. Top-view FE-SEM images of as-deposited γ-$CsPbI_3$ films with layer varying CsI thickness: (a) 200, (b) 300, (c) 400, and (d) 500 nm. Grain size and surface uniformity of the fabricated films improve with increasing CsI thickness.

decrease in film dislocation from 6.17×10^{-9} to 1.69×10^{-9} nm^{-2} with increasing CsI thickness. Films with CsI thicknesses of 400 and 500 nm CsI showed improved dislocation density, suggesting compatible stoichiometric ratios for fabricating a suitable $CsPbI_3$ absorbing layer. This observed trend aligns well with the phase transition from cubic (α-$CsPbI_3$) to the orthorhombic structure (γ-$CsPbI_3$), demonstrated by Yang et al. [50].

Moreover, Hyder and co-workers [40] conducted an analytical study on the effect of dislocation density on the performance of InGaN-based multi-junction solar cells. Their observations suggested that dislocation density directly affects open-circuit voltage (Voc), short-circuit current (Isc), power conversion efficiency (PCE), and the minority carrier lifetime. Applying this analogy, the film with a 400 nm CsI thickness, observed with the least dislocation density, is expected to produce good optoelectronic properties, improving the PCE for solar cells.

Table 1
Variation of average grain size grown by SPVD for varied CsI thicknesses.

CsI Thickness (nm)	Average grain size As-deposited (nm)	Average grain size Annealed (nm)
200	208	169
300	239	237
400	185	190
500	178	170

3.2 Field-emission scanning electron microscopy

3.2.1 Surface morphology analysis of as-deposited $CsPbI_3$ thin films

Fig. 5 shows the $CsPbI_3$ (PbI_2:CsI) thin film's surface morphology synthesized by SPVD for varying CsI thicknesses. Micrographs depicted in Fig. 5(a) reveal that the film exhibits a densely packed, granular structure with uniform, randomly orientated, and pin-hole free grains. The compact grains suppress trap state densities at GBs, enhancing charge carrier mobility [41], which is beneficial for efficient charge transport in solar cells. Also, uniform grain size can reduce electron-hole recombination and enhance the PCE of the solar cell. In Fig. 5(b), the grains of 300 nm CsI thickness appear larger and more irregular as compared to the 200 nm CsI thickness. However, the film displays more voids and gaps between the grains, which may presumably increase current leakage. Nonetheless, large grains can improve light absorption. In contrast, the voids might hinder charge transport, potentially reducing the efficiency, whereas passivation may necessarily improve surface morphology. Liu et al. [38] used an amino-grouped polyhedral oligomeric silsesquioxane to passivate trap states, which improved the device PCE, Voc, and cell stability. Consequently, we expect the reduction in grain boundaries to result in improved cell stability. The thin film displayed in Fig. 5(c) shows even larger and more irregular grains than the 300 nm CsI thickness film. Furthermore, the GBs are more distinct, demonstrating excellent pathways for charge carriers. The observed large grains also demonstrate the onset requirement of CsI thickness to suppress the residues of excess PbI_2 at GBs. This effect is known to enhance carrier lifetime and produce better Voc, Jsc, and fill-factor (FF) improving the solar cell performance. On the other hand, Fig. 5(d) depicts slightly more irregular shapes and sizes with distinct GBs, suggesting a balance between light absorption and charge transport, potentially offering a good performance in solar cells. Overall, the films demonstrated that the grain size increases with an increase in CsI thickness. Calculated average grain sizes with varying CsI thicknesses are given in Table 1.

3.2.2 Surface morphology for annealed $CsPbI_3$ thin films

Fig. 6 displays γ-$CsPbI_3$ surface morphology grown by SPVD for various CsI thicknesses. The micrographs reveal that the films exhibit a polycrystalline structure with closely packed grains. These grains appear to have a slightly polygonal shape, which is typical for perovskite thin films. Therefore, this morphology suggests good crystallization of the γ-$CsPbI_3$ phase. The grain sizes appear relatively uniform for the varying CsI thickness, with an average diameter of approximately 170 to 237 nm. This grain size is within the favourable range for $CsPbI_3$ PSCs [42], as it can provide a good balance between charge transport and recombination dynamics. Moreover, the films exhibit uniform surface coverage, with evenly distributed grains across the imaged areas. This confirms that varying the annealing time from 0 to 10 min also has a negligible impact on the grain size. However, according to a study done by Yonezawa et al. [43], annealing time plays a fundamental role in achieving effective intercalation of CsI into PbI_2 while ensuring perfect transformation into γ-$CsPbI_3$ with full-surface-covered morphologies. There are some variations in grain size and larger grains with visible clusters, particularly in Fig. 6(a) and (d).

Overall, annealing produced good surface coverage without pinholes or large void films, depicting potential improvement in device performance. Studies have proven that bulky compact pin-hole free surface morphologies are the result of a high absorption coefficient for perovskites [44]. Furthermore, some visible brighter spots, particularly in Fig. 6(a) and (d), could indicate surface roughness or the presence of secondary phases. Subsequently, we observed that the GBs are visible across the films displayed in Fig. 8(a)–(d). These GBs are mostly visible in Fig. 6(b), which displays relatively larger grains according to Table 1. Therefore, in good interpretation, the above-studied SEM surface topographies indicated in Figs. 5 and 6 demonstrated excellent grain-size properties, required for high solar cell efficiency, with satisfying surface coverage. Besides the nature of the surface topographies, a crucial fact is that the morphology of IOPs is interdependent on the GBs, compositional non-uniformity, phase impurity/purity, interface, good surface morphology, etc. Thus, surface morphology with sufficiently large grain size, uniformly distributed, and pinhole-free properties is still in high demand to boost the future of perovskite-based solar cells towards

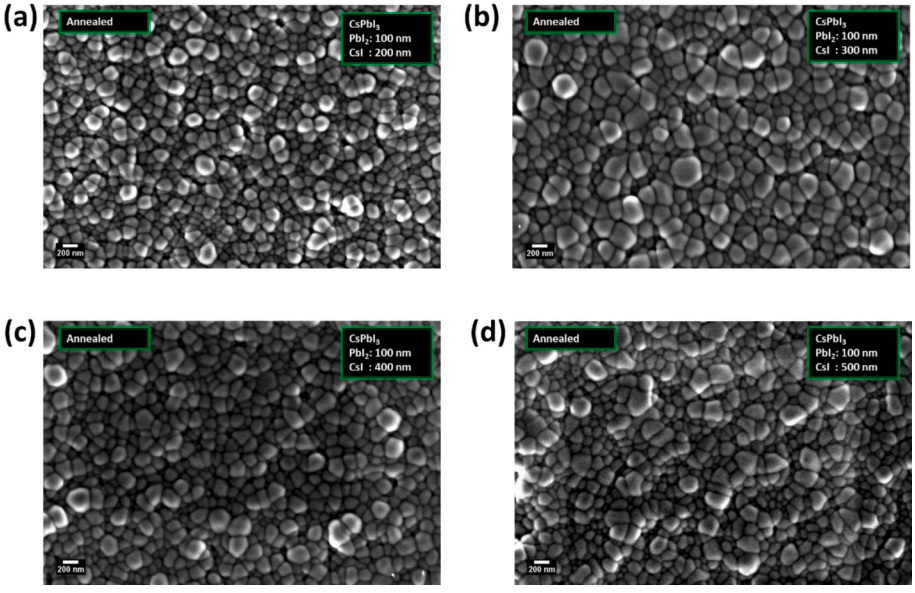

Fig. 6. Top-view FE-SEM images of γ-$CsPbI_3$ films annealed at 100 °C with CsI thickness of (a) 200, (b) 300, (c) 400, and (d) 500 nm. Films exhibited compact, polygonal grains with good surface coverage and reduced defects.

commercialization. Fig. 7 compares the average grain sizes with varying CsI thickness from 200 to 500 nm and the image colors for as-deposited and annealed at 400 nm CsI thickness.

3.3 Ultraviolet–Visible Spectroscopy

Fig. 8(a) depicts the visible-light absorption properties of the as-deposited thin film measured from 500 to 800 nm wavelengths. The absorption spectra show distinct absorptions at 526, 534, and 544 nm. These absorption intensities vary with CsI thickness, while the 300 nm CsI film depicts the highest absorption intensity. This observation complements the light absorption properties of the large grains discussed in Fig. 5(b). Furthermore, Fig. 8(b) demonstrates the effect of annealed $CsPbI_3$ thin films at 100 °C. The absorption spectra exhibit significant changes compared to the as-deposited films, which include new absorption peaks at 534, 554, and 560 nm. In addition, there is an observed broader red shift peak at around 634 nm, which is not present in the as-deposited thin films. Therefore, it is evident that the overall absorption intensity increases notably after annealing, particularly for the 300 nm thin film. Annealing treatment improves the perovskite structure significantly as depicted by the red shift, broadening absorption spectrum, the emergence of new absorption peaks, and a slight reduction in bandgap energies. These changes suggest that annealing promotes better crystallization, potentially larger grain sizes, and possibly a change in perovskite phase or composition, all of which contribute to enhanced light absorption properties of the thin films. Fig. 8(c) and (d) show estimated bandgaps from Tauc's plot for as-deposited and annealed thin films with varying CsI thicknesses. Fig. 8 (a) shows that the absorption edge shifts to higher energies as CsI thickness decreases, with the bandgaps ranging from 2.28 to 2.38 eV. Moreover, upon annealing, a similar trend is observed, but the absorption edges shift to slightly lower energies (2.05 to 2.37 eV), indicating the narrowing of the bandgap. These calculated bandgaps are consistent with the reported literature values for the most stable room temperature $CsPbI_3$ polymorph (orthorhombic phase) [45]. Therefore, it is worth noting that the large bandgaps observed in this type of perovskite are believed to be a result of the common octahedral tilting phenomena. Similar octahedral tilting [46] and subsequent increases in bandgap have been widely observed for inorganic hybrid perovskites [47].

3.4 Atomic force microscopy analysis

We further examined the morphologies of the inorganic perovskite thin films on FTO using atomic force microscopy (AFM) to investigate the effect of varying CsI thickness. The surface topographies of $CsPbI_3$ thin films for 300, 400, 500, and 600 nm are shown in Fig. 9(a)–(d). The measured surface roughness values were 44.0, 40.7, 38.3, and 39,6 nm for CsI precursors of 200, 300, 400, and 500 nm, respectively. Films with low CsI thickness displayed high surface roughness as illustrated in Fig. 9(a) and (b). Furthermore, surface-mapping demonstrated a reduction in the films' roughness with an increase in CsI thickness, reaching a less rough optimal thickness of 400 nm of CsI depicted in Fig. 9(c). Furthermore, the top-view 3D lateral inset images show morphology correlation with the SEM, indicating the grain size reaches a maximum when the CsI thickness is 300 nm. However, the surface roughness is relatively large. This phenomenon is due to the nucleation of crystals occurring on the surface of FTO. Subsequently, the crystal grains grew rapidly, resulting in higher surface roughness. Once the roughness reached its maximum at a film thickness of 400 nm $CsPbI_3$, additional deposition of CsI nanoparticles filled the voids of surface impurities and thereby reduced the overall surface roughness as observed for the 600 nm (Fig. 9(d)) and 500 nm. Nonetheless, the 500 nm $CsPbI_3$ film thickness displays the lowest surface roughness, demonstrating the highest film quality amongst all the films, which is in good agreement with the XRD, UV–Vis, and SEM results. Moreover, the decrease in surface roughness trend indicates the effect of varying CsI thickness.

3.5 Electrical properties

3.5.1. FTO/c-TiO_2/perovskite/LiF/Au electron-only devices

Electrical characterizations were subsequently conducted to investigate further the effect of varying the CsI thickness of $CsPbI_3$ thin films on electrical properties. The device architecture is displayed in Fig. 10 (a). FTO/c-TiO_2/$CsPbI_3$/LiF/Au demonstrates an electron-only device used for photoelectrical measurements. Fig. 10(b) shows the semi-logarithmic I-V curves for varied CsI thicknesses, whilst Fig. 10(c) and (d) demonstrates dark and illuminated semi-logs of the device's response.

3.5.2. Trap states and electron mobility for $CsPbI_3$ electron-only based devices

We further studied the effect of varying CsI from 200 – 500 nm, using electrical characterization to assess the density of trap states for 300, 400, 500, and 600 nm $CsPbI_3$ thin films, with a focus on examining defect densities of the perovskite films. Fabricated electron-only device based on FTO/c-TiO_2/perovskite/LiF/Au architecture is displayed in Fig. 11(a). The applied voltage at the kink point, known as trap-filled limit voltage (V_{TFL}), is used to evaluate the density in trap states, as described by the following equation:

$$V_{TFL} = \frac{eN_tL^2}{2\varepsilon_o\varepsilon} \tag{5}$$

where *e, Nt, L,* ε_o, and ε stand for the elementary charge, the density of trap states, the film thickness, the vacuum permittivity, and the dielectric constant, respectively. The regime where the current increases linearly as a function of voltage up to the kink point indicates an ohmic response (Ohmic region). Fig. 11(a)–(d) shows the ohmic region below n-values = 1.027, 1.058, 1.000, 0.357 for the 300, 400, 500, and 600 nm

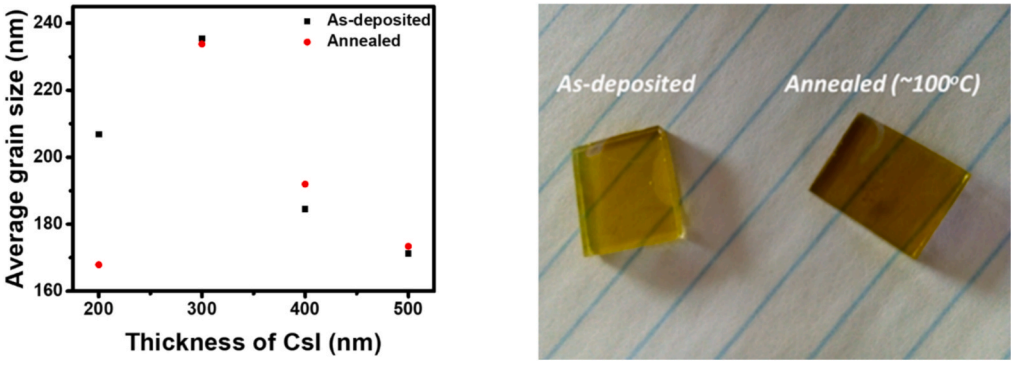

Fig. 7. Comparison of average grain size and optical image coloration of as-deposited and annealed $CsPbI_3$ with varying CsI thickness (200 – 500 nm).

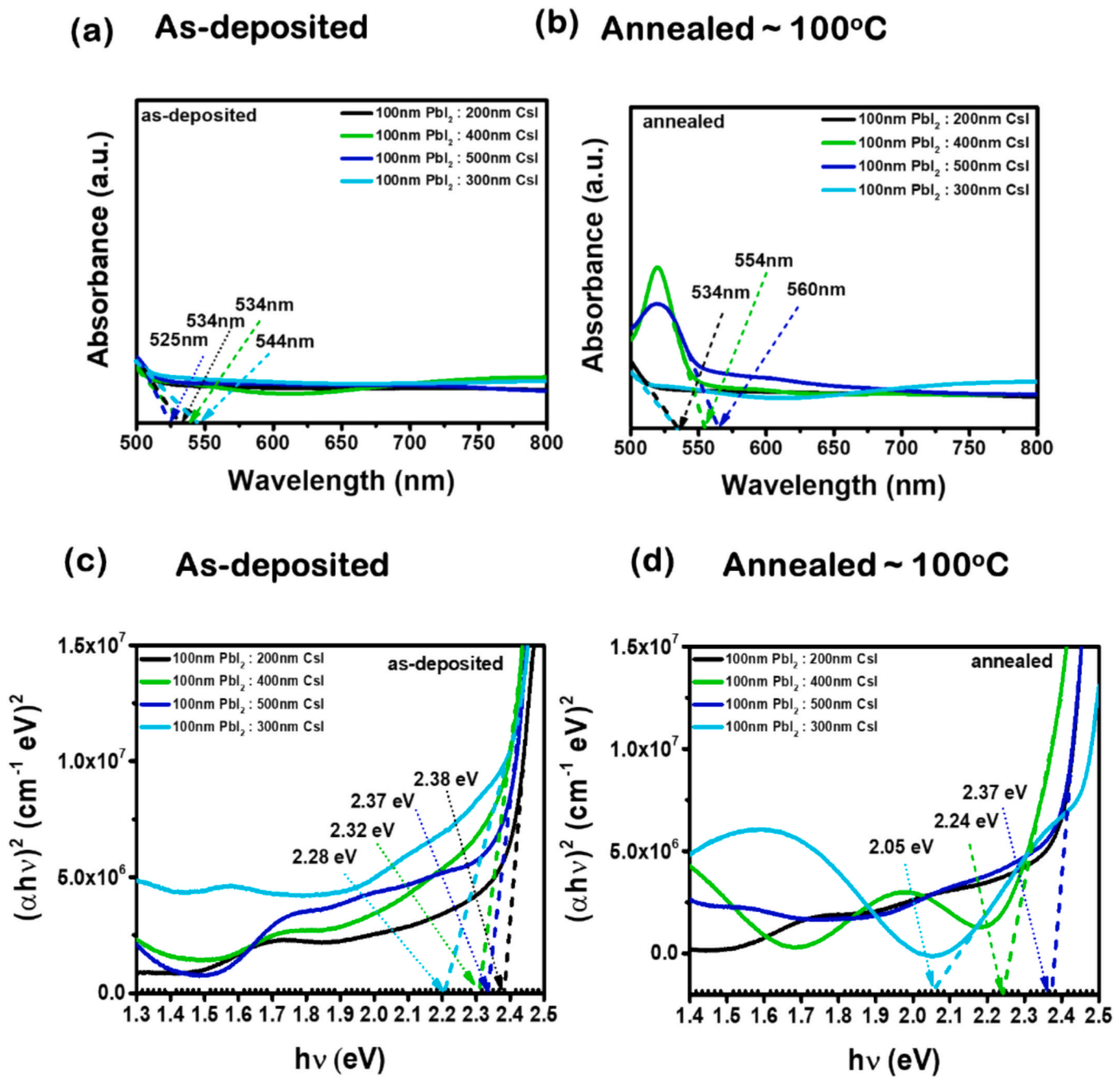

Fig. 8. (a) UV–Vis absorbance spectra of as-deposited $CsPbI_3$ films. (b) Absorbance spectra upon 100 °C annealing conditions. (c) and (d) Tauc plots estimating optical bandgaps for as-deposited and annealed films, respectively.

$CsPbI_3$-based electron-only devices, respectively. The trap-limited current (TLC) observed after the ohmic regimes by the slopes higher than 2 (slope of space-charge limited current) in a log–log plot, clearly indicates the immobilization of charge carriers (electrons), thus the trap states. Motley-Gurney's square law demonstrated the slope of 2 using a single-carrier current in a device on a high forward bias [61]. Voltage dependence of the TLC was 0.288, 0.285, 0.549, and 1.541 V for 300, 400, 500, and 600 nm $CsPbI_3$-based devices, respectively. Therefore, this suggests that the 600 nm device (with a stronger V_{FTL}) suffers from deeper depth of traps, demonstrated by the steeper slope in the FTL regime. Calculated trap states in Fig. 11(a) 1.40×10^{15}, (b) 9.84×10^{15}, (c) 1.21×10^{14}, and (d) 8.31×10^{14} cm^{-3}, respectively, agree with the results depicted by V_{FTL} values and indicate a decreasing trend of defect density as CsI thickness is increased. Furthermore, the 600 nm exhibited a higher trap depth than the 500 nm $CsPbI_3$-based device, suggesting higher dark-current density loss, as depicted by the semi-log plot in Fig. 10(d). Moreover, the device in Fig. 11(a) displayed similar attributes in a low voltage dependence current and low n_{traps}, suggesting shallow traps close to the transport band energy, demonstrated by the high dark current leakage of $\sim 10^{-5}$ Amps. These phenomena further indicated a major disadvantage in the device's PCE performance. On the other hand, increasing CsI thickness from 200 to 500 nm demonstrated a directly proportional relationship between the trap-filling limit voltage and the defect density. According to Wang et al. [48], higher V_{TFL} reduces the photogenerated charge carrier's mobility, consequently affecting the device's performance and resulting in a low PCE.

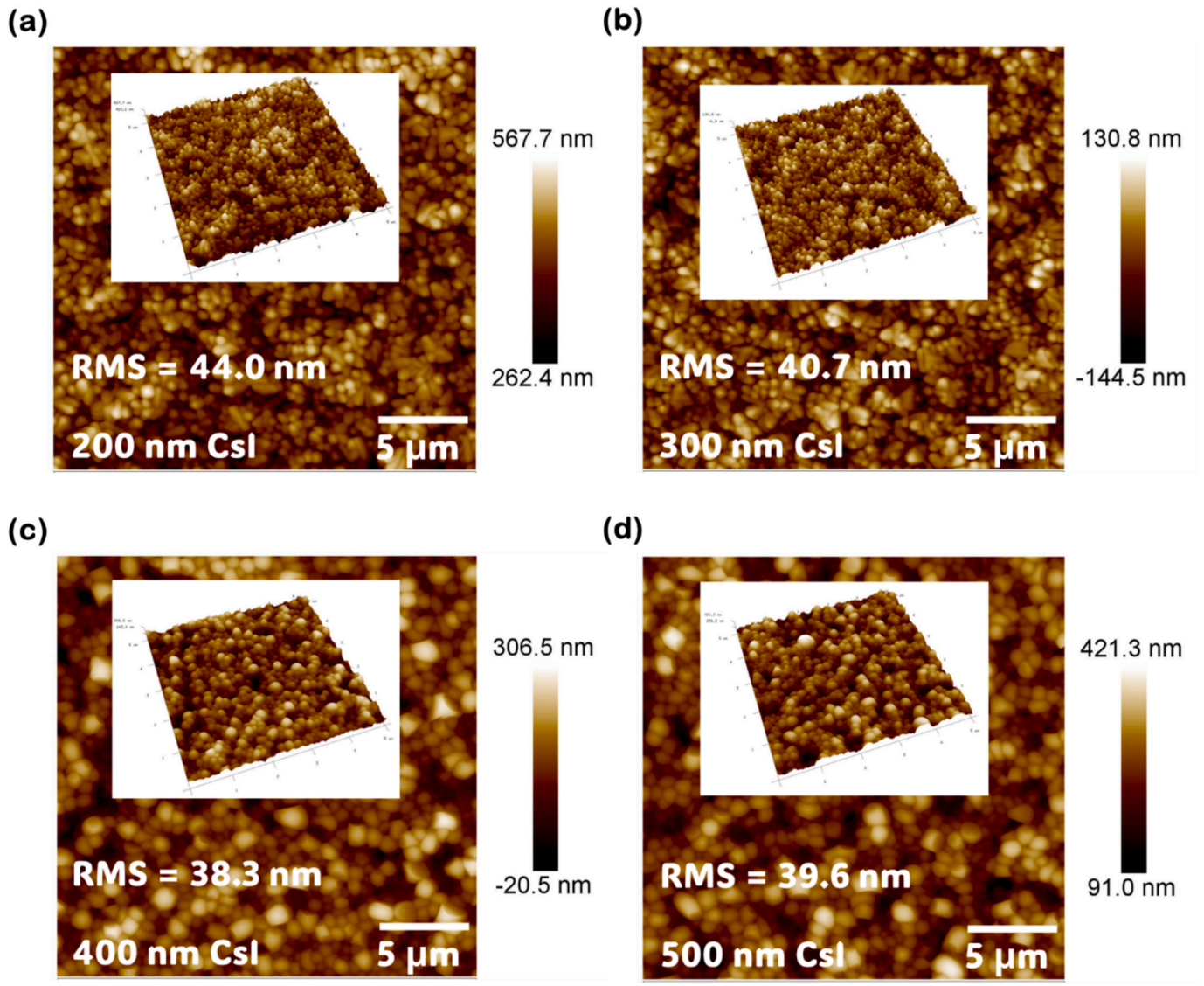

Fig. 9. AFM surface topography of $CsPbI_3$ films with CsI thicknesses of (a) 200, (b) 300, (c) 400, and 500 nm. Insets show 3D topography maps with decreasing surface roughness as CsI thickness increases (200 – 500 nm).

3.5.3. FTO/c-TiO_2/$CsPbI_3$/Au devices

Fig. 12(a) and (b) display the fabricated FTO/c-TiO_2/$CsPbI_3$/Au device's architecture and energy band diagram. Fig. 13(a)–(d) shows J-V (current density–voltage) characteristics of hole-transport-free inorganic-halide PSCs with an n-i-p configuration, focusing on the FTO/c-TiO_2/$CsPbI_3$/Au device's architecture, with varying $CsPbI_3$-based thickness. Varying the thickness demonstrates the importance of film optimization and the influence of CsI thickness on the device's PCEs for the all-inorganic-halide PSCs. Fig. 13(a) demonstrates a solar cell based on a 300 nm CsI thickness having a low Voc = 0.27 eV as a result of the minimum film thickness limit for PSCs. This low Voc can be attributed to the small-scattered grain size displayed in Fig. 6(a), clearly demonstrating major optical losses due to poor electrical contact (resulting in martensite-green contact) at the n-type interface with 5 – 15 % loss of sunlight. Furthermore, the cell demonstrates high recombination effects (low Voc) incurred from the density of trap states in the transition region, which agrees with the 20.40 mA/cm^2 high Jsc (see, Table 2), and the significant dark current leakage (loss) shown in Fig. 13(b) resulting in the 2.0 % PCE PSC's response. Nevertheless, an increment in CsI thickness to 400 nm PSC thickness, displayed an improved Voc = 0.97 eV by a factor of 3.6, thus demonstrating effective suppression of possible recombination rate of charge carriers as an attribute to the larger grain size (Fig. 6(b)), reduced bandgap (Fig. 10(d)), and less current leakage (Fig. 13(b)). Consequently, the device's 4.49 % PCE is lower than that of 500 and 600 nm film's thickness, which may be the result of the 9.84×10^{15} cm^{-3} defect depth being larger than that of 500 and 600 nm $CsPbI_3$ by a factor of 1.5 and 1.6, respectively. Therefore, the resulting highest 4.93 % PCE for the bulky 500 nm $CsPbI_3$-based device could be due to the good crystallinity (Fig. 2(a) and (b)) of the optimal 400 nm CsI thickness, attributed to the SPVD technique used by Fru et al. [49] for the synthesis of $MAPbBr_3$ thin films through vacuum-assisted evaporation. The technique demonstrated good ETL, and active layer inter-diffusion as shown by the low density of trap states of 1.21×10^{14} cm^{-3}, dark-current leakage (Fig. 10(b)), bulk, and surface charge recombination rates deduced from the Voc increment (from 0.27 – 0.75 eV) in comparison to the 300 nm $CsPbI_3$ film. This cell further demonstrated improved electrical contact and better light response (Fig. 12(e)), which may be the result of the bulk larger grain sizes shown in Fig. 6(c). In contrast, the $CsPbI_3$ 600 nm film thickness PSC showed a reduction in PCE of 4.04 %, demonstrating the threshold of CsI thickness. This phenomenon is further indicated by the reduction in crystal growth displayed in Fig. 2(b). The device demonstrates a good Voc as an

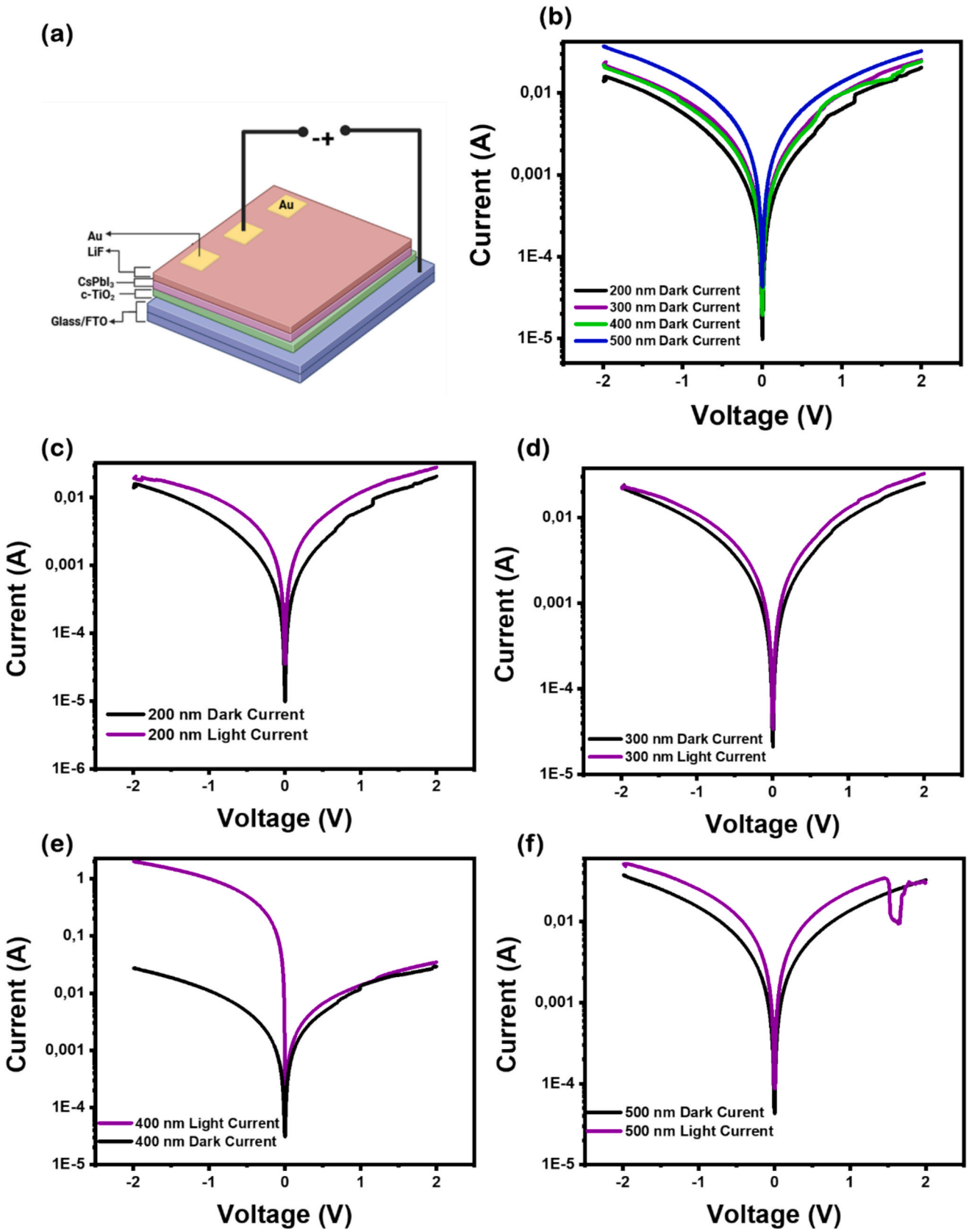

Fig. 10. (a) Device architecture of FTO/c-TiO_2/perovskite/LiF/Au electron-only device for SCLC measurements. (b) Semi-log I-V characteristics of $CsPbI_3$ thin films under dark current for varied CsI thickness (200 – 500 nm). (c) and (d) Comparison of dark and illuminated I-V curves, highlighting photoresponse behavior.

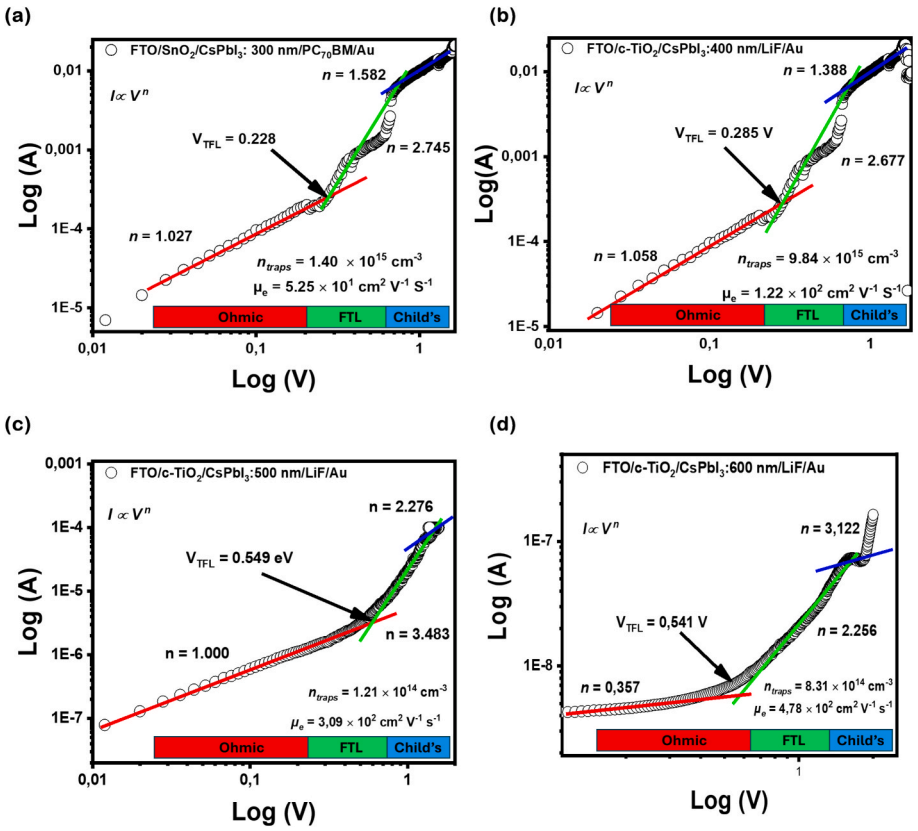

Fig. 11. Dark I-V curves for electron-only device with $CsPbI_3$ layers at varying CsI thicknesses: (a) 300, (b) 400, (c) 500, and (d) 600 nm films. Curves demonstrate variation in trap-filled limit voltages and trap state densities.

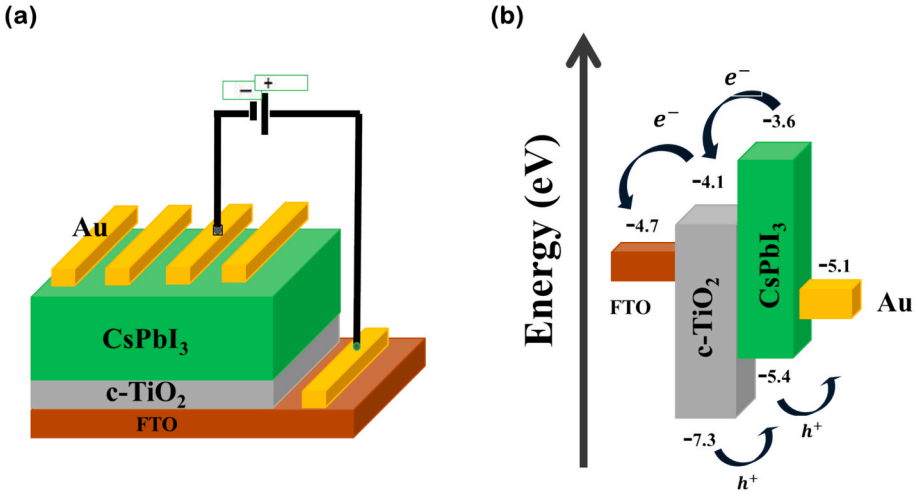

Fig. 12. Schematic illustration of HTL-free device architecture: FTO/c-TiO_2/$CsPbI_3$/Au. (b) corresponding energy band diagram illustrating charge transport mechanism of the fabricated all-inorganic perovskite solar cells.

attribute to a lower surface charge carrier recombination rate; however, further investigations suggest higher density of trap states 8.31 × $10^{14}cm^{-3}$ (Fig. 11(d)), deducing a major site of charge recombination centers and thus the dark current leakage (see Fig. 13(b)), compromising the PSC's performance. This efficiency due to better Voc, shows an improved FF of 41.98 % subject to the better shunt (Rsh) and series (Rs) resistances, and possibly optimal interface contacts causing the semi-log shape of the scan as illustrated in Fig. 13(d). Higher Rsh attenuates the Jsc and therefore influences the current leakage. Following Ohm's law, the leakage current through Rsh can be expressed as in Equation (6):

$$J_{sh} = \frac{V - JRs}{Rs} \tag{6}$$

where Jsh, V, JRs, and Rs represent shunt current, voltage, series resistor current, and series resistance, respectively. The curves suggest reasonable fill factors, indicating good charge transport properties in agreement with the VTL slopes indicated in Fig. 11(a)–(d). Furthermore, this study contributes to understanding thickness-dependent performance in all-inorganic perovskite solar cells, which is crucial for optimizing device efficiency and stability.

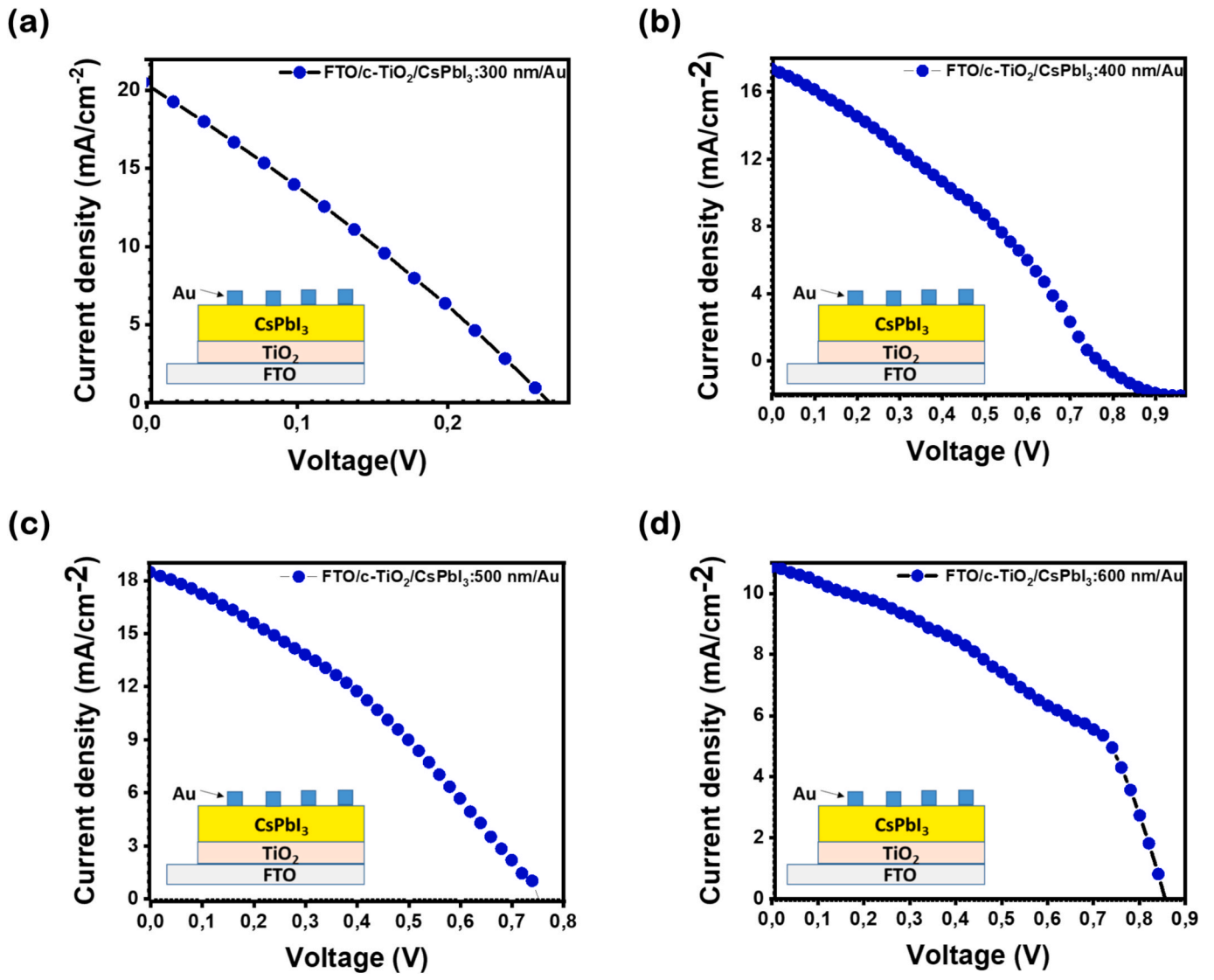

Fig. 13. J-V characteristics of $CsPbI_3$-based PSCs with varying CsI thickness: (a) 300, (b) 400, (c) 500, and (d) 600 nm, after 100 °C thermal treatment, and measured under illuminated conditions.

Table 2
Photovoltaic parameters of I-V measurements under-illumination for $CsPbI_3$ solar cells with varying CsI thicknesses.

CsI Thickness (nm)	V_{OC} (V)	J_{SC} (mA/cm^2)	R_{SH} (Ω/cm^2)	R_S (Ω/cm^2)	FF (%)	PCE (%)
200	0.27	20.40	15402.53	10294.93	28.05	2.00
3.00	0.96	17.29	91070.25	42496.66	26.85	4.49
400	0.75	18.66	107117.80	22691.65	36.24	4.93
500	0.88	10.89	888333.00	31718.28	41.98	4.04

4 Conclusion

In this study, we successfully demonstrated the growth and characterization of γ-$CsPbI_3$ thin films using the SPVD technique. The films, deposited on c-TiO_2-coated FTO substrates, exhibited good crystallinity, phase stability, and uniform surface coverage, resulting in a favourable interface with the ETL and enabling an efficient electron extraction pathway. The optimized HTL-free device, fabricated with a 400 nm CsI thickness, achieved a PCE of up to 4.93 %, Voc = 0.75 V, Jsc = 18.66 mA/cm^2, and a fill factor of 36.24 %.

When compared to Mayimele et al.'s work [50], which reported a lower PCE of 2.13 % for a $MAPbI_3$-based HTL-free solar cell also fabricated via SPVD, our γ-$CsPbI_3$based device demonstrates superior performance, highlighting the advantage of all-inorganic perovskites in terms of thermal stability and optoelectronic quality. It is worth noting, however, that both studies employed HTL-free architectures. Therefore, as part of future work, we plan to integrate a suitable HTL into the device stack to facilitate efficient hole extraction and improve overall performance.

This study primarily focused on the optimization of structural, morphological, optical, and electrical properties of $CsPbI_3$-based PSCs using a reproducible SPVD technique. The findings reinforce the potential of SPVD for producing stable, fully inorganic perovskite films with promising optoelectronic properties. Furthermore, the relatively large bandgap of γ-$CsPbI_3$ makes it a suitable candidate for the top cell in tandem photovoltaics. Future work will also explore surface passivation to promote larger, more compact grain growth and perhaps bandgap reduction, thereby enhancing light absorption and photogeneration for better performance.

CRediT authorship contribution statement

Sizwe Sibiya: Writing – original draft, Methodology, Investigation,

Formal analysis, Data curation, Conceptualization. **Mmantsae Diale:** Writing – review & editing, Supervision, Resources, Project administration.

Declaration of competing interest

The authors declare that they have no known competing financial interests or personal relationships that could have appeared to influence the work reported in this paper.

Acknowledgments

The authors wish to thank the University of Pretoria and NRF-South Africa, grant no 115463 of the SARChI, for financial support. We also acknowledge Prof. JM Nel for the well-appreciated assistance with AFM measurements.

Data availability

Data will be made available on request.

References

[1] S. De Wolf, et al., Organometallic halide perovskites: sharp optical absorption edge and its relation to photovoltaic performance, J. Phys. Chem. Lett. 5 (6) (2014) 1035–1039.
[2] T. Kirchartz, et al., Impact of small phonon energies on the charge-carrier lifetimes in metal-halide perovskites, J. Phys. Chem. Lett. 9 (5) (2018) 939–946.
[3] P. Umari, E. Mosconi, F. De Angelis, Infrared dielectric screening determines the low exciton binding energy of metal-halide perovskites, J. Phys. Chem. Lett. 9 (3) (2018) 620–627.
[4] Y. El Ajjouri, et al., Tunable wide-bandgap monohalide perovskites, Adv. Opt. Mater. 8 (17) (2020) 2000423.
[5] Z. Yang, et al., Enhancing electron diffusion length in narrow-bandgap perovskites for efficient monolithic perovskite tandem solar cells, Nat. Commun. 10 (1) (2019) 4498.
[6] C. Liu, et al., Interphases, interfaces, and surfaces of active materials in rechargeable batteries and perovskite solar cells, Adv. Mater. 33 (22) (2021) 1905245.
[7] L. Clinckemalie, et al., Challenges and opportunities for CsPbBr3 perovskites in low-and high-energy radiation detection, ACS Energy Lett. 6 (4) (2021) 1290–1314.
[8] A. Nur'aini, I. Oh, Volatile organic compound gas sensors based on methylammonium lead iodide perovskite operating at room temperature, RSC Adv. 10 (22) (2020) 12982–12987.
[9] J.J. Yoo, et al., Efficient perovskite solar cells via improved carrier management, Nature 590 (7847) (2021) 587–593.
[10] M. Khalid, T.K. Mallick, Stability and performance enhancement of perovskite solar cells: a review, Energies 16 (10) (2023) 4031.
[11] Q. Wang, et al., Enhancement in lifespan of halide perovskite solar cells, Energ. Environ. Sci. 12 (3) (2019) 865–886.
[12] H. Syafutra, et al., Surface degradation mechanism on CH3NH3PbBr3 hybrid perovskite single crystal by a grazing E-beam irradiation, Nanomaterials 10 (7) (2020) 1253.
[13] I. Mesquita, L. Andrade, A. Mendes, Effect of relative humidity during the preparation of perovskite solar cells: performance and stability, Sol. Energy 199 (2020) 474–483.
[14] P. Liu, et al., High-quality Ruddlesden–Popper perovskite film formation for high-performance perovskite solar cells, Adv. Mater. 33 (10) (2021) 2002582.
[15] X.-T. He, et al., A silicon-on-insulator slab for topological valley transport, Nat. Commun. 10 (1) (2019) 872.
[16] J. Philipp, et al., Structural and doping effects in the half-metallic double perovskite A 2 CrWO 6 (A= Sr, Ba, and Ca), Phys. Rev. B 68 (14) (2003) 144431.
[17] J. Liang, et al., CsPb0. 9Sn0. 1IBr2 based all-inorganic perovskite solar cells with exceptional efficiency and stability, J. Am. Chem. Soc. 139 (40) (2017) 14009–14012.
[18] P.K. Nayak, D. Ghosh, Optimizing excited charge dynamics in layered halide perovskites through compositional engineering, Nano Lett. 25 (13) (2025) 5520–5528.
[19] K. Wang, et al., Chlorine doping for black γ-CsPbI3 solar cells with stabilized efficiency beyond 16%, Nano Energy 58 (2019) 175–182.
[20] S. Ullah, F. Khan, J.F. Rasheed, Prospects for commercialization of CsPbIBr2-based all-inorganic perovskite solar cells: fabrication, stability, and engineering strategies, Adv. Funct. Mater. (2025) 2503508.
[21] J. He, et al., Influence of phase transition on stability of perovskite solar cells under thermal cycling conditions, Sol. Energy 188 (2019) 312–317.
[22] Q. Wang, et al., Scaling behavior of moisture-induced grain degradation in polycrystalline hybrid perovskite thin films, Energ. Environ. Sci. 10 (2) (2017) 516–522.
[23] F. Ji, et al., Simultaneous evolution of uniaxially oriented grains and ultralow-density grain-boundary network in CH3NH3PbI3 perovskite thin films mediated by precursor phase metastability, ACS Energy Lett. 2 (12) (2017) 2727–2733.
[24] A.F. Castro-Méndez, J. Hidalgo, J.P. Correa-Baena, The role of grain boundaries in perovskite solar cells, Adv. Energy Mater. 9 (38) (2019) 1901489.
[25] M. Beygisangchin, et al., Advancements in configuration structures and fabrication techniques for achieving stability in perovskite solar cells: a comprehensive review, J. Korean Ceram. Soc. 61 (5) (2024) 755–782.
[26] J.V. Patil, S.S. Mali, C.K. Hong, Exceeding 23% efficiency for 3D/3D bilayer Perovskite heterojunction MAPbI3/FAPbI3-based hybrid perovskite solar cells with enhanced stability, Adv. Funct. Mater. 35 (1) (2025) 2408721.
[27] F. Haque, et al., Effects of hydroiodic acid concentration on the properties of CsPbI3 perovskite solar cells, ACS Omega 3 (9) (2018) 11937–11944.
[28] A.K. Singh, et al., Unlocking all-perovskite tandem solar cells to∼ 30% efficiency: a simulation and optimization approach with MPA2FPh-BT-BA as a hole selective contact, J. Opt. 54 (1) (2025) 96–105.
[29] S. Wang, et al., Over 24% efficient MA-free CsxFA1− xPbX3 perovskite solar cells, Joule 6 (6) (2022) 1344–1356.
[30] A. Mujtaba, et al., Enhanced the efficiency of TMs (Co and Ag) doped lead based mixed halides perovskite solar cells through the conduction band gap engineering, J. Indian Chem. Soc. 102 (4) (2025) 101618.
[31] F. Bella, et al., Caesium for perovskite solar cells: an overview, Chem. Eur. J. 24 (47) (2018) 12183–12205.
[32] T. Gallet, et al., Co-evaporation of CH3NH3PbI3: how growth conditions impact phase purity, photostriction, and intrinsic stability, ACS Appl. Mater. Interfaces 13 (2) (2021) 2642–2653.
[33] M.I. Pintor Monroy, et al., All-evaporated, all-inorganic CsPbI3 Perovskite-based devices for broad-band photodetector and solar cell applications, ACS Appl. Electron. Mater. 3 (7) (2021) 3023–3033.
[34] R. Heidrich, et al., Impact of dynamic co-evaporation schemes on the growth of methylammonium lead iodide absorbers for inverted solar cells, Sci. Rep. 12 (1) (2022) 19167.
[35] J.-A. Yang, et al., Precise control of PbI2 excess into grain boundary for efficacious charge extraction in off-stoichiometric perovskite solar cells, Electrochim. Acta 338 (2020) 135697.
[36] A. Alberti, et al., Pb clustering and PbI2 nanofragmentation during methylammonium lead iodide perovskite degradation, Nat. Commun. 10 (1) (2019) 2196.
[37] N. Wang, Y. Wu, Intrinsic defects on α, γ and δ-CsPbI 3 (001) surfaces and implications for the α/γ to δ phase transition, PCCP 25 (23) (2023) 16077–16085.
[38] N. Liu, et al., Extremely low trap-state energy level perovskite solar cells passivated using NH 2-POSS with improved efficiency and stability, J. Mater. Chem. A 6 (16) (2018) 6806–6814.
[39] G. Williamson, R. Smallman III, Dislocation densities in some annealed and cold-worked metals from measurements on the X-ray debye-scherrer spectrum, Phil. Mag. 1 (1) (1956) 34–46.
[40] S. Hyder, M. Wilkov, Effect of dislocation density on the epitaxial growth of silver, J. Appl. Phys. 38 (5) (1967) 2386–2387.
[41] Y. Hu, et al., Understanding the role of cesium and rubidium additives in perovskite solar cells: trap states, charge transport, and recombination, Adv. Energy Mater. 8 (16) (2018) 1703057.
[42] Y. Fu, et al., Selective stabilization and photophysical properties of metastable perovskite polymorphs of CsPbI3 in thin films, Chem. Mater. 29 (19) (2017) 8385–8394.
[43] K. Yonezawa, et al., Annealing effects on CsPbI3-based planar heterojunction perovskite solar cells formed by vacuum deposition method, Jpn. J. Appl. Phys. 56 (4S) (2017) 04CS11.
[44] A.K. Jena, A. Kulkarni, T. Miyasaka, Halide perovskite photovoltaics: background, status, and future prospects, Chem. Rev. 119 (5) (2019) 3036–3103.
[45] B. Wang, N. Novendra, A. Navrotsky, Energetics, structures, and phase transitions of cubic and orthorhombic cesium lead iodide (CsPbI3) polymorphs, J. Am. Chem. Soc. 141 (37) (2019) 14501–14504.
[46] R. Prasanna, et al., Band gap tuning via lattice contraction and octahedral tilting in perovskite materials for photovoltaics, J. Am. Chem. Soc. 139 (32) (2017) 11117–11124.
[47] J.-H. Lee, et al., Resolving the physical origin of octahedral tilting in halide perovskites, Chem. Mater. 28 (12) (2016) 4259–4266.
[48] K. Wang, et al., Beach-chair-shaped energy band alignment for high-performance β-CsPbI3 solar cells, Cell Rep. Phys. Sci. 1 (9) (2020).
[49] J. Fru, N. Nombona, M. Diale, Characterization of sequential physical vapor deposited methylammonium lead tri-iodide perovskite thin films, Vacuum 182 (2020) 109727.
[50] M. Mayimele, et al., Sequential physical vapor deposited methylammonium lead tri-iodide perovskites on FTO and ITO modified zinc oxide nanorods for perovskite solar cells, Phys. B Condens. Matter 625 (2022) 413462.